Single-electron source based on ultra-short voltage pulses for flying-electron qubits

Master Thesis Report

Matteo ALUFFI

Internship supervisor: Christopher BÄUERLE

Academic tutor: Giancarlo CICERO

Academic year 2022-2023

ALUFFI Matteo

Master 2 student
Politecnico di Torino
Nanotechnologies for ICTs
Corso Duca degli Abruzzi, 24,
10129 Torino TO, Italia

3rd year engineering student
Grenoble INP Phelma
Ingénierie Physique pour la photonique
et la microélectronique
3 parvis Louis Néel
38 000 Grenoble, France
s290290@studenti.polito.it

M2 internship performed at the Néel Institute under the supervision of Christopher Bäuerle and in collaboration with professor Giancarlo CICERO.

Bäuerle Christopher

Research director
Institut Neel - CNRS
25 avenue des Martyrs
38 042 Grenoble, France

christopher.bauerle@neel.cnrs.fr

CICERO Giancarlo

Full professor
Politecnico di Torino
24 Corso Duca degli Abruzzi
10129 Torino, Italy

giancarlo.cicero@polito.it

Abstract

The demand for ever-increasing computational power cannot be met anymore by the advancement of microelectronics. Quantum computing present itself as the solution to this problem, with multiple qubit platform being currently under development. The flying electron qubit architecture appears to be a promising candidate due to its potential for scalability. However, the technology is still in its infancy and several building blocks are still missing, among which a reliable single electron source.

In this work, the leviton single electron source will be extensively studied. Two different techniques for the generation of ultrashort electron wave packets will be presented. Finally, a record-short electron wave packet will be characterised while propagating in a 2DEG.

Acknowledgements

My first thanks go to my parents, for supporting me during these long years of study, and to my sister, for being a great inspiration in my life and for sharing with me the coffe breaks during the exams.

I would like to thank my internship supervisor Christopher Bäuerle for accepting me as an internship student and for welcoming me in the institute. He has been a great teacher and I am looking forward to work with him again in the future.

I am grateful to professor Gianciarlo Cicero for his guidance in the redaction of this report and in the preparation of the final defense.

The last thanks go to Clément Geffroy, Mohamed Seddik Ouacel, Jun-Liang Wang and Aymeric Richard for the patience demonstrated in teaching me during this internship and for being incredible friends.

Contents

List of Figures

Glossary

2DEG: Two-dimensional electron gas
SES: Single electron source
GaAs/AlGaAs: Gallium arsenide/ Alluminium gallium arsenide
LT-GaAs: Low-temperature grown gallium arsenide
HEMT: High electron mobility transistor
QD: Quantum dot
SEM: Scanning electron microscope
IDT: Interdigited transducer
SAW: Surface acoustic wave
FWHM: Full width at half maximum
AWG: Arbitrary waveform generator
DFT: Discrete Fourier transform
RF: Radio frequency
BPF: Band-pass filter
VCA: Voltage-controlled attenuator
VCPS: Voltage-controlled phase-shifter
DAC: Digital to analog converter
ADC: Analog to digital converter
MZI: Mach-Zehnder interferometer
QPC: Quantum point contact
TCW: Tunnel coupled wire

Introduction

In the last century, the development of microelectronics has allowed for the design of devices with incredibly large computational power. However, the progress in the field seems to be reaching its limit [1]. Many computationally intensive problem that even with the best supercomputer would take thousands of years to solve still remains unanswered. A new computational paradigm is needed in order to overcome this problem.

Quantum computing proposes to solve this problem by encoding the information in the quantum state of a particle [2]. By exploiting the quantum superposition of the states of multiple particles, an exponentially large computational power is achieved. Many platforms for the implementation of quantum computing have been proposed, each exploiting the characteristic of a different physical system [3–10].

A interesting platform is the flying-electron qubit, where information is encoded in the position of one electron and is processed as it flies through the system [9]. Multiple technological challenges still have to be solved before implementing the flying-electron in a quantum computer. One of these challenges is the development of a highly efficient and coherent single electron source. This can be realized by generating a short voltage pulse of a specific waveform, which will constitute the core of this report.

In the following, after a brief discussion about the flying-electron qubit architecture, we will focus our attention on the leviton single-electron source. Firstly, the theoretical background of leviton excitations will be presented. We will then study a radio frequency pulse generator able to generate levitons with a temporal width of 20 picoseconds. This will be followed by the characterisation of an electron wave-packet propagating in the 2DEG of a GaAs heterostructure. Finally, we will discuss an alternative approach for the generation of voltage pulses with a temporal width down to one picosecond, based on optoelectronic conversion.

Chapter 1

State of the art

1.1 Quantum computing

The fundamental building block of all quantum architectures is the "Qubit" [2]. For most quantum technologies, a qubit is composed of a two-level system, where depending on the technology it can be a Josephson junction (superconducting qubits) [7], the presence or absence of a photon or an electron in a waveguide (photonic and electronic flying qubits) [3, 9], the spin state of an electron (spin qubits) [8] or simply the energy state of an atom (trapped ion qubits) [4]. Let us consider a qubit to be a system with two quantum states, denoted by $|0\rangle$ and $|1\rangle$. The state of such a quantum system can be described by a superposition of these two states:

$$|\psi\rangle = cos(\theta/2)\,|0\rangle + e^{i\varphi} sin(\theta/2)\,|1\rangle \tag{1.1}$$

This superposition can be graphically represented by a Bloch sphere, as shown in figure 1.1. Quantum computers are predicted to perform computations exponentially faster than conventional high-performance computers, simply by exploiting this superposition of states. To experimentally realise qubits, it is necessary to perform operations such that every point on the Bloch sphere can be addressed. These are the so-called single qubit rotations. To perform logic operations, a two-qubit gate is also necessary [2].

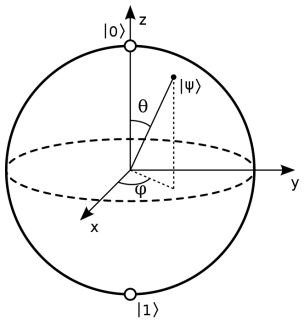

Figure 1.1: Bloch sphere representation. The angles θ and φ fully describe the superposition of states.

1.2 GaAs/AlGaAs heterostructures

Flying electron qubits, in analogy to photonic qubits, rely on electron waveguides, beam splitters and phase shifters. These fundamental building blocks of electron quantum optics are realised by high mobility, doped GaAs/AlGaAs heterostructures (HEMTs) [11]. The quality of HEMTs is of paramount importance for maintaining the coherence of electron flying qubits, since the presence of impurities can lead to electron scattering and therefore its decoherence. To form high quality HEMT structures, a layer of Silicon (Si)-doped Aluminum Gallium Arsenide (n-AlGaAs) is grown by molecular beam epitaxy on top of an intrinsic GaAs substrate. Because of the differences in the work functions and energy gaps of the two materials, the free electrons are able to diffuse from their Si-donors in n-AlGaAs into the GaAs. As shown in figure 1.2(a), due to the electric field that is created by the deserted Si-donors and the discontinuity in the energy gap, a potential minimum is formed at the boundary of the two semiconductors. Electrons will eventually be trapped in a triangular potential well formed at the interface. This layer is named a two dimensional electron gas (2DEG), as electrons can only move freely along the boundary between the GaAs and n-AlGaAs semiconductors. Since no dopants are present in the GaAs, where the 2DEG is formed, electrons are protected from ionized impurity scattering, which greatly increases their mobility and coherence time [12].

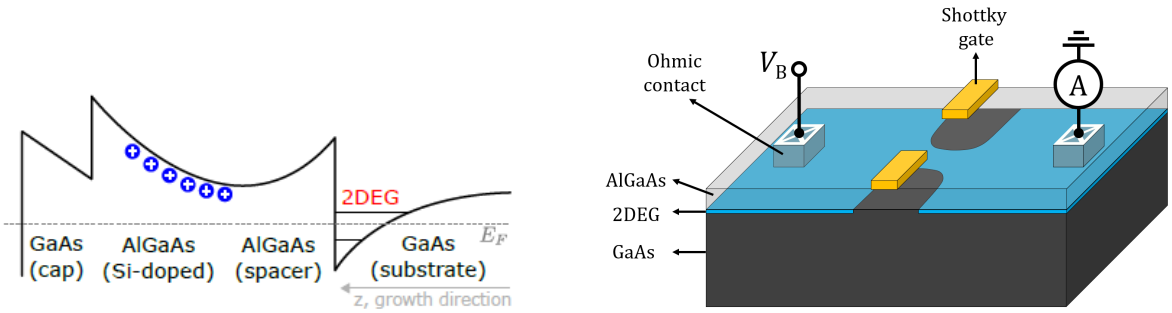

Figure 1.2: GaAs/AlGaAs heterostructure. a) Heterostructure energy band diagram. A 2DEG is formed by a triangular potential at the interface of GaAs and AlGaAs semiconductors. b) Example of patterning a 2DEG with Schottky gates. Adapted from [13].

By depositing metallic Schottky gates on top of the GaAs heterostructure, it is possible to tailor the geometry of the 2DEG at will [14], as shown in 1.2(b). When a sufficiently negative voltage is applied to the gate, the electrons beneath are repelled by the generated electrostatic field and the 2DEG is locally depleted. It is hence possible to modify the morphology of the 2DEG to create sophisticated structures, such as electron interferometers, or quantum dots by simply patterning Schottky gates on the

surface of the AlGaAs.

To be able to control the motion of the electrons in the 2DEG, an electric field must be applied. To this purpose, ohmic contacts have been developed [15]. These contacts are made by depositing a metal alloy of gold, germanium and nickel on the surface of the AlGaAs. When the contact is annealed at high temperature, the metals form an euthetic alloy with the AlGaAs, which diffuses downward, deep in the semiconductor. Eventually, it will touch the 2DEG and form an ohmic path between the electron gas and the surface. By appropriately placing an ohmic contact, it is possible to inject or detect electrons in the 2DEG.

All these building blocks allow the study of the coherent motion of electrons in an arbitrarily shaped 2-dimensional system. This is a relatively new research field and it is called "electron quantum optics" [16].

1.3 Flying electrons qubits

By appropriately patterning a 2DEG with Schottky gates, it is possible to define electronic waveguides, beam splitters and phase shifters with equivalent functionality to their photonic analogues. In its most basic form, a flying electron qubit is made of a propagating electron within two identical electronic waveguides, as illustrated in figure 1.3. The qubit states, $|0\rangle$ and $|1\rangle$, are defined by which channel is occupied by the electron during its flight, either the top arm or the bottom arm [17].

To create a superposition between the two states, the two waveguides are brought close to each other and a small, tuneable energy barrier is placed in between them, also shown as "tunnel barrier" in figure 1.3. By tuning the barrier height with an applied gate voltage, we can control the superposition state of the qubit, which corresponds to a rotation by an angle θ on the Bloch sphere, figure 1.3(b). In practice, this changes the tunnelling probability of the electron between the two waveguides and allows for the electron wave packet to be arbitrarily split. This configuration is also know as a tunnel-coupled wire and it is equivalent to the photonic directional coupler, or beam splitter [9].

To completely control the state of an electronic flying qubit, we need to implement a rotation by an additional angle ϕ on the azimuthal plane of the Bloch sphere. A rotation by ϕ is understood as a phase shift between the two superposed states. To implement an electronic phase shifter, the two waveguides are separated into two arms with the region between them being depleted by a Schottky gate, figure 1.3(c) The phase shift between the two paths, upper and lower, is controlled by the intensity of an externally applied magnetic field. Due to the Aharonov-Bohm effect [18], the phase shift introduced between the upper and lower path is proportional to the intensity of the magnetic field and the surface area enclosed by the two paths. As shown in 1.3(d), this phase shift is equivalent to a rotation of an angle ϕ on the Bloch sphere.

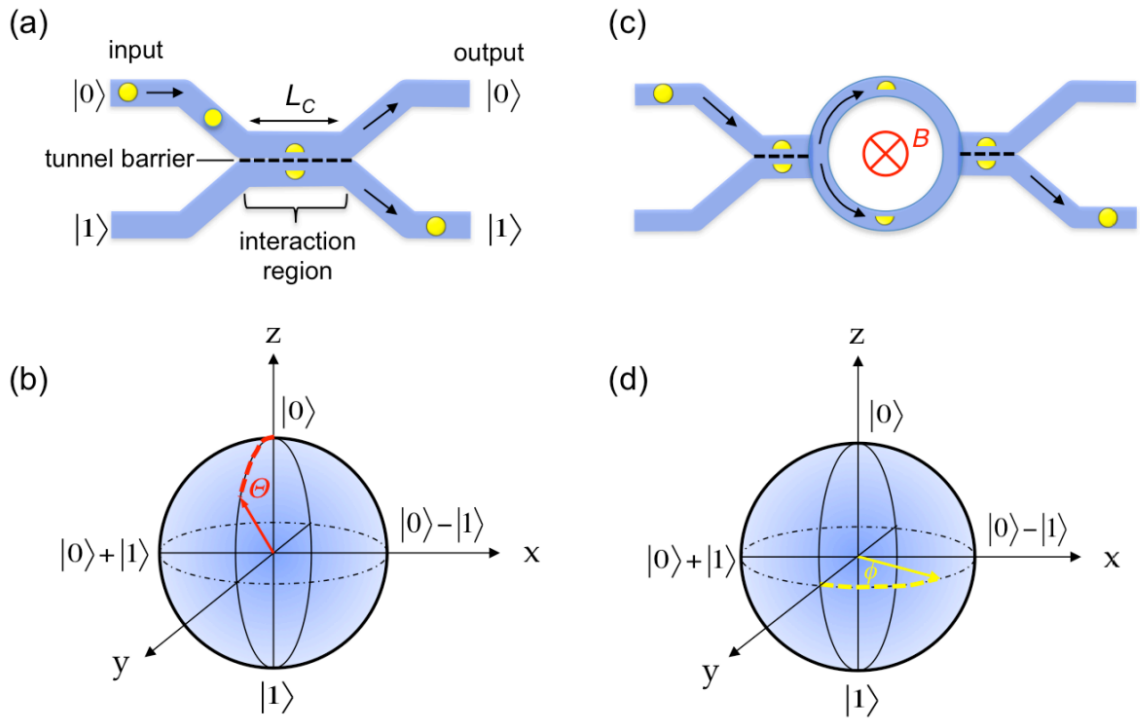

Figure 1.3: Operation of a flying electron qubit. a) An electron (yellow dot) is propagating through an electronic waveguide (blue). Two waveguides are brought together to allow partial tunneling between them, forming a tunnel-coupled wire. b) The Bloch sphere rotation induced by the tunnel-coupled wire. c) The two channels are separated to enclose a surface where a perpendicular magnetic field is present, inducing a phase difference between the upper and lower path. d) Bloch sphere rotation induced by the Aharonov-Bohm effect. Picture adapted from [9].

The two paths can finally be brought together to observe the interference between the electron wave packets, effectively creating the electronic counterpart of a two path Mach-Zehnder interferometer.

With these two simple building blocks, a tunnel barrier and a Aharonov-Bohm ring, any qubit states on the Bloch sphere can be obtained while the electrons fly through the system. This qubit architecture has one great advantage with respect to many of his counterparts. The devices are integrated on a single GaAs chip, which provides an easy platform for the up-scaling of the technology [17]. However, many technological challenges must be solved before exploiting the flying electron qubit in a quantum computer. Most importantly, a reliable single electron source is still to be developed.

1.4 Single electron sources

One of the biggest challenges for the flying electron qubit architecture is the ability to generate on-demand single-electrons. For this purpose, different single-electron sources (SESs) have been developed throughout the years. In what follows, the most popular SESs will be presented.

1.4.1 Non-adiabatic single electron pump.

The non-adiabatic single electron source was developed for metrology purposes to serve as a current standard [19–21]. Figure 1.4(a) shows a scanning electron microscope (SEM) image of the device. It consists of a quantum dot whose energy barriers are controlled by two Schottky gates.

The operation principle of this electron source is shown in figure 1.4(b). Initially, (1) the entrance barrier (left side) is lowered and multiple electrons enter the quantum dot and occupy the energy levels below the Fermi energy. Subsequently, (2) the entrance barrier is slowly raised while keeping the exit barrier (right side) fixed. This will increase the energy of the electrons inside the dot while excess electrons will tunnel back to the reservoir. The size of the quantum dot is optimised such that eventually only one electron is left trapped in the potential minimum (3). The electron is then isolated in the quantum dot region, by raising the entrance barrier even further. As a result, (4) the energy of the trapped electron increases until the electron escapes the dot through the exit gate.

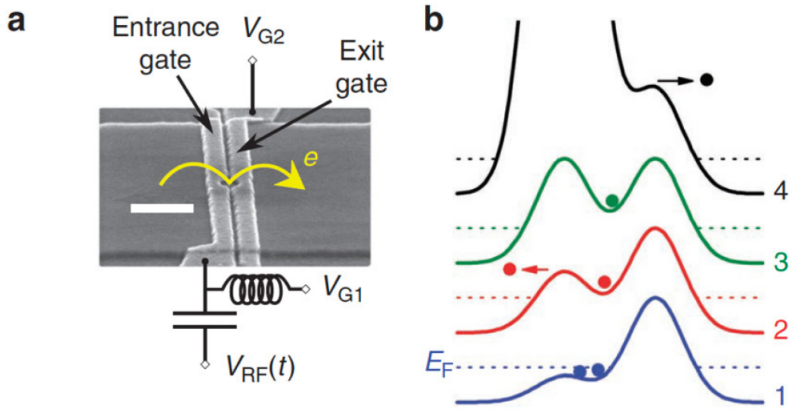

Figure 1.4: Non-adiabatic single electron pump. a) SEM image of the single electron pump. b) Evolution of the energy barriers during the pump operation. Picture adapted from [19].

Since the single electron pump reliably generates a single electron per cycle, the generated current is $I = ef$, where f is the operating frequency of the entrance gate. At a repetition frequency of 1 GHz, a precise current of 160 pA is generated and owning

to its unique accuracy this source is used as a current standard [22]. However, the electrons generated from this source are emitted with a relatively high energy above the Fermi sea, (100 meV) [23]. This can greatly impact electron coherence time, as the electron will eventually scatter to the lowest energy state, thus making this source unsuitable for quantum information technologies.

1.4.2 Mesoscopic capacitor SES

The mesoscopic capacitor is conceptually very similar to a single electron pump [24]. The operating sequence of the device is shown in figure 1.5. A quantum dot, defined by three metallic gates, is used to capture electrons from the Fermi sea. The separation between the energy levels of the quantum dot are arranged to be high enough to prevent thermal excitations between them. In this situation, the first energy level below the Fermi sea is occupied by exactly one electron, and the first level above is completely empty (1). By applying on the quantum dot a periodic square pulse (top left in figure 1.5), the energy levels of the quantum dot are lifted. The amplitude of the pulse is chosen such that the first energy level of the dot below the Fermi sea is lifted to the next unoccupied energy level, just over the Fermi sea. The electron will tunnel through the barrier and inject on top of the Fermi sea (2). By returning to the initial state (3), the empty energy level of the dot captures an electron from the Fermi sea, and as a consequence a hole is emitted from the source (3).

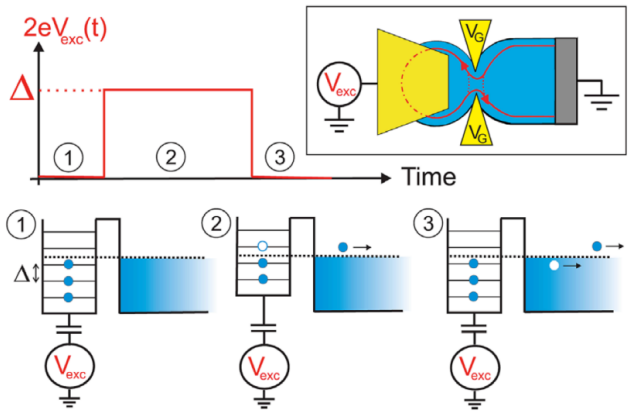

Figure 1.5: Working principle of the mesocopic capacitor SES (1) A mesoscopic capacitor is in thermal equilibrium with the Fermi sea. The Fermi energy is situated between two energy levels of the quantum dot. (2) A voltage is applied to raise the highest occupied level above the Fermi energy. The electron contained in this level is injected in the edge state circulating within the QD in the Fermi sea. (3) The voltage is removed and the emptied energy level is once again below the Fermi energy. An electron is recalled to fill it, effectively generating a hole in the Fermi sea. Picture adapted from [25].

The quantum dot and the applied voltage can be tuned in order to reduce the electron emission energy down to a few meV. This greatly increases the coherence time of the electron, but the additional generation of a hole during the operation makes the mesoscopic capacitor less suitable for quantum information technologies [26]. Additionally, since the device will generate an average current equal to zero, it cannot be used as a current standard for metrology application.

1.4.3 Moving quantum dot as SES

An alternative possibility to build single electron sources is using a "moving" quantum dot [27, 28]. The device is shown in figure 1.6 (a) and it operates as follows. Initially, a single electron is trapped in a quantum dot defined by three electrostatic gates (red, green and blue), depicted on the left side of figure 1.6 (a). By exploiting the piezoelectric effect of GaAs, a surface acoustic wave (SAW) is generated by an interdigitated transducer (IDT) and is sent towards the quantum dot. Because of the inverse piezoelectric effect, the SAW generates a moving electric field that propagates with the wave. When the SAW reaches the quantum dot, the electron is collected by the electric field and is trapped in a moving potential energy minimum. The electron propagates with the SAW until it is catched by a second quantum dot (right side of figure 1.6(a)), where a very sensitive electrometer allows for single-shot electron detection [29].

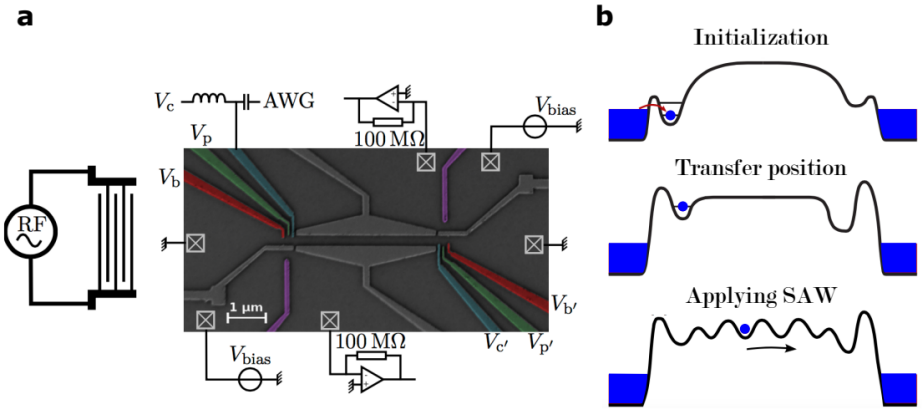

Figure 1.6: Single electron source based on surface acoustic waves. a) SEM image of a sample used for a SAW-based single-electron transport experiment. b) Potential energy landscape seen by the electron during SAW transport. Picture adapted from [28].

The coherence properties of the electrons emitted from this electron source are yet to be studied. A serious concern is represented by the lack of a Fermi sea that would otherwise screen Coulomb interactions between the travelling electron and the charge fluctuations in the electrostatic gates [30]. In any case, SAW-based single electron

sources have demonstrated incredible reliability in the generation, transport and detection of a single electron [28]. Flying electron qubits based on this technology are currently under development [31].

Finally, a single electron source can also be implemented by generating single electron excitations directly on top of the Fermi sea. This SES represent the core of this report and it will be extensively introduced in chapter 2.

Chapter 2

Leviton single electron source

In the previous section, different approaches for the quantum dot based generation of single electrons have been presented. In the following we will present an extensive theoretical treatment of leviton SES. This will be followed by a description of how we can experimentally generate such Lorentzian voltage pulse necessary for the generation of levitons. We will see that an important parameter for the manipulation of the single electron excitation is the temporal width of the wave packet. We will show 2 different approaches to generate short voltage pulses. One very versatile method of Fourier synthesis using radio frequency technology which is limited to a wave packet width of 20 ps and a second much more elaborate method which is based on opto-electronic conversion. With the latter approach we aim to generate wave packets with temporal extension down to one picosecond.

2.1 Theory

In a 2DEG, electrons composing the Fermi sea can be described by a plane wave $\Psi(x,t) = e^{ikx-iEt/h}$ [32]. Locally applying a voltage pulse will add an extra phase to the wavefunction:

$$\Psi(x,t) = e^{i\phi(t)+ikx-iEt/h}, \tag{2.1}$$

with the phase $\phi(t)$:

$$\phi(t) = \int_{-\infty}^{t} \frac{eV(t')}{\hbar} dt'. \tag{2.2}$$

Notice that equation 2.2 provides a powerful tool to control the phase of the electron's wavefunction with a macroscopic quantity like a voltage.

We are now interested in computing the effect of a voltage pulse on the electron's energy distribution. Assuming the initial state to have an energy ϵ_f, the probability to find an electron at an energy $\epsilon_f + \Delta\epsilon$ can be computed with Floquet scattering theory

as [33]:

$$P(\Delta\epsilon) = \frac{1}{2\pi\hbar}\left|\int_{-\infty}^{\infty} e^{-i\phi(t)}e^{it\Delta\epsilon/\hbar}dt\right|^2 = \frac{1}{2\pi\hbar}\left|\mathscr{F}\{e^{-i\phi(t)}\}(\omega = -\Delta\epsilon/\hbar)\right|^2, \tag{2.3}$$

where $\mathscr{F}$ denotes the Fourier transform. With equation 2.3 it is now possible to look for a voltage pulse $V(t)$ such that $P(\Delta\epsilon) = 0$ when $\Delta\epsilon < 0$. This condition ensures that when the pulse is applied to the Fermi sea, only electronic states are excited above the Fermi level (i.e. $\Delta\epsilon > 0$), while no hole is generated in the sea below ($\Delta\epsilon < 0$). The absence of holes greatly increases the coherence length of the system as hole decoherence is one of the main perturbing effects [26].

Solving for the pulse shape is a very complex variational problem that has been solved only in 1996 by Levitov et al. [34, 35]. The resulting voltage pulse is:

$$V(t) = -\frac{nh}{e\pi}\ \frac{\frac{1}{2}\Gamma}{(t-t_0)^2 + \frac{1}{4}\Gamma^2}, \tag{2.4}$$

where n is a natural number, t_0 is the central position of the pulse and Γ is the full width at half maximum (FWHM) of the Lorentzian pulse. In the same paper, Levitov showed that the absence of holes persist even if multiple pulses are applied to the Fermi sea, regardless of the relative time delay between them.

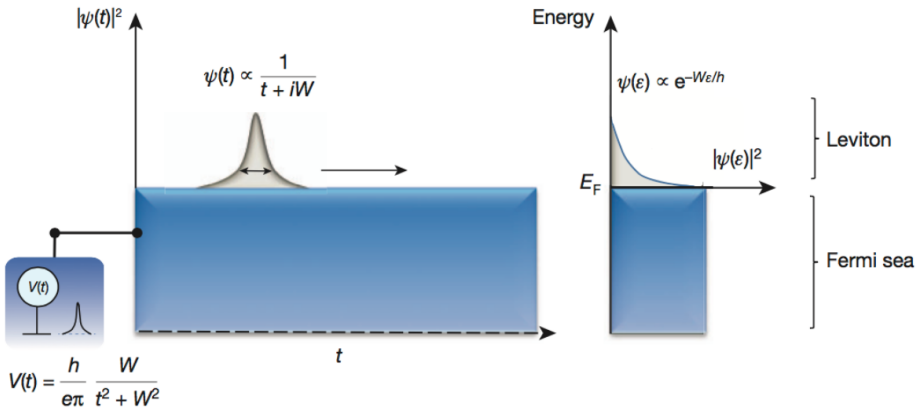

Figure 2.1: On the left: single-electron Lorentzian pulse (gray) propagating on top of the Fermi sea (blue). On the right: Electron energy distribution (gray) respect to the Fermi sea (blue). Picture adapted from [36]

The resulting excitation spectrum is shown in figure 2.1 and consist in exponentially-vanishing probability just a few tens of μeV (for pulses of the order of 100 ps) above the Fermi level. By living close to the Fermi sea, levitons are screened by the surroundings electrons and we expect that this increases their phase coherence. Moreover, since the states above the Fermi level are continuously occupied, energy relaxation should be inhibited.

It is now interesting to consider a one dimensional conductor with quantized conductance $G = e^2/h$ to which we apply a Lorentzian pulse as described in equation 2.4. The number of electrons displaced by the voltage can be easily computed as:

$$N_e = -\frac{1}{e}\int i(t)dt = -\frac{1}{e}\int GV(t)dt = \frac{e}{h}\int \frac{nh}{e\pi}\ \frac{\frac{1}{2}\Gamma}{(t-t_0)^2+\frac{1}{4}\Gamma^2} = n \tag{2.5}$$

Recalling that $n \in \mathbb{N}$, an incredibly remarkable property of Lorentzian pulses is obtained: no holes are generated in the Fermi sea if and only if the pulse displaces exactly an integer number of electrons. It is then sufficient to set $n = 1$ to have an efficient and reliable way of generating and transporting a single electron in a 1D conductor. For this amazing feature, this excitation takes the name of Leviton, in honour of the scientist who first described it.

For $n \notin \mathbb{N}$, a random number of holes and electrons are generated at each pulse and n is no longer the number of electrons displaced by each pulse, but it is instead representative of the average number of displaced charges $n = \langle N_e - N_h \rangle$. The fluctuating charge significantly increases the current noise, which provides a way of experimentally distinguish a leviton current from a normal RF one [36].

While Lorentzian pulses seems to consist an efficient single-electron source, one last constraint has to be taken into account before exploiting levitons in a quantum logic circuit. Every manipulation of the electronic state must be performed before the information about the initial phase is destroyed, which means that the leviton should not propagate for more than a phase-relaxation length L_ϕ. For electrons in a GaAS/AlGaAs heterostructure the typical coherence length is of the order of 100 µm [17]. Supposing a system of 50 logic elements, the coherence length limits the size of each element to 2 µm, which must be larger than the size of the electron pulse propagating at the Fermi velocity $v_f \approx 10^5\ \mathrm{m\,s^{-1}}$. The temporal width of the pulse is then also limited to $\Delta t = 2\,\mu\mathrm{m}/v_f \approx 20\,\mathrm{ps}$, which greatly increases the complexity of experimental setups as the electronics has to work in the THz regime.

In this section, the theory behind single-electron pulses has been presented. Starting from the application of a generic voltage pulse to the Fermi sea, the electronic excitation spectrum has been computed, and the lack of holes generation has been demonstrated for particular Lorentzian-shaped pulses. Successively, the number of electrons transported by each pulse have been investigated alongside the challenge imposed by the required THz electronic.

In the next chapter, a first radio-frequency approach for the generation of ultrashort Lorentzian pulses will be presented.

Chapter 3

Radio-frequency Fourier synthesis of Lorentzian pulses

In the preceding chapter we have shown that a Lorentzian voltage pulse will generate a pure electronic excitation within the Fermi sea without the generations of any holes. In this section we will outline how such Lorentzian voltage pulse can be generated experimentally. This is by no means a simple task as wave packets of a temporal width of a few tens picoseconds have to be generated. Even the best commercially available arbitrary waveform generators (AWG) can only sample a point each 20 ps, which would mean only two to three points per pulse. In this section, we will present how we overcame the problem with a different type of signal generator based on Fourier synthesis.

3.1 Fourier synthesis

Any periodic, square integrable function can be decomposed as a superposition of sine waves with a Fourier series:

$$f(t) = \sum_{n=0}^{\infty} A_n \, sin(nf_0 t + \phi_n), \tag{3.1}$$

where $f(t)$ is a periodic function of frequency f_0, and A_n and ϕ_n are the amplitude and phase of the n^{th} harmonic. Equation 3.1 can also be understood in the following way: it is possible to reproduce a generic periodic function by simply adding sinusoidal waves with the adequate amplitude and phase.

In a real application it is not possible to add an infinite number of harmonics and thus only an approximation of the desired function is obtained:

$$\tilde{f}(t) = \sum_{n=0}^{N} A_n \, sin(nf_0 t + \phi_n) \tag{3.2}$$

The error over one period between the desired function and the synthesised one, can be computed with L^2 norm as:

$$\left\| f(t) - \tilde{f}(t) \right\| = \sum_{n=N+1}^{\infty} \pi A_n^2 \tag{3.3}$$

Equation 3.3 suggest that, in order to have a good approximation of the desired function, the amplitude A_n should be rapidly vanishing. This condition is particularly true for trigonometric polynomials, whose spectrum has a limited support, and for a Gaussian and Lorentzian functions, for which the Fourier spectrum is exponentially vanishing for higher harmonics. Since we have previously shown that a superposition of Lorentzian pulses still generates levitons without any hole excitation, we can efficiently exploit Fourier synthesis to generate periodically-spaced single-electron pulses.

3.2 RF synthesis based on a frequency comb.

In order to perform the Fourier synthesis of a signal, it is necessary to control every parameter in equation 3.2. A radio frequency system has all the necessary building blocks to perform the needed actions, from multiple way of generating a high number of frequencies, to phase-shifters and attenuators for complete control of each harmonics.

3.2.1 Working principle

The device developed in the group to perform the Fourier synthesis has been inherited from the former internship student Thomas Vasselon, who assembled it and wrote the first version of the control code.

The block diagram is shown in figure 3.1. A continuous-wave signal generator injects a 3 GHz (19 dBm) sinusoidal signal into a MARKI NLTL 6026 microwave frequency comb, consisting of a GaAs Schottky diode. Owing to its non-linear characteristics, higher harmonics of the fundamental frequency are generated up to 60 GHz. We expect that by having all the harmonics to share a single common source, the output signal will be very stable in time.

The signal is then evenly split into 8 different lines, each provided with a band-pass filter to select a specific harmonic from 3 GHz to 24 GHz. Each harmonic is sent through a voltage-controlled attenuator and phase-shifter to control the amplitude and phase. In order to determine the voltages to be applied to the attenuators and phase-shifters, the output waveform is measured with a sampling oscilloscope. A Python control program extracts the phase and amplitude of the harmonics of the recorded trace with a discrete Fourier transform (DFT). Then the voltages applied through the DAC are changed in order to match the spectrum of the requested signal. It is also possible to compensate for the dispersion of a system by simply applying to this

spectrum the inverse transfer matrix. Since acting on the attenuator will also introduce a phase shift, the process must be iterated multiple time until convergence. A minute is the typical time needed to complete the optimisation.

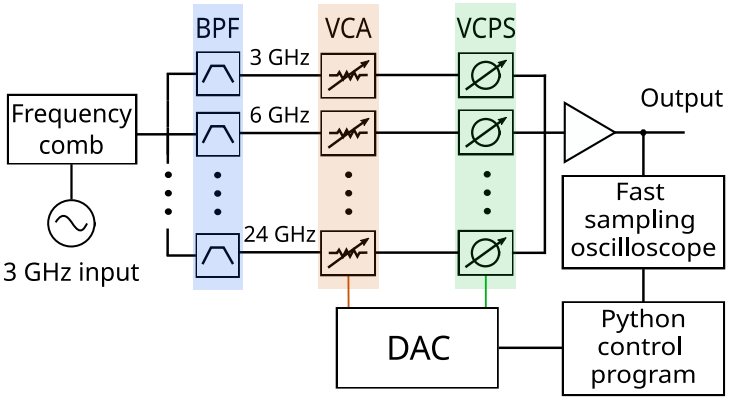

Figure 3.1: Pulse generator's block diagram. The 3 GHz input signal is sent through the frequency comb to generate higher harmonics. A bank of band-pass filters (BPF) selects each harmonic. Voltage-controlled attenuators (VCA) and phase-shifters (VCPS) allow to adjust the amplitude and phase of each frequency. The harmonics are then recombined at the output to generate the desired waveform. A computer program controls the attenuators and phase shifter using a feed-back loop by analysing the waveform recorded on the sampling oscilloscope. Reproduced from [37].

3.3 Results

While the device could theoretically output an approximation of any waveform, we will mostly focus our attention on Lorentzian pulses. In figure 3.2 a few Lorentzian output with progressively increasing width (FWHM) are shown. It is interesting to notice how for shorter widths the pulse does not perfectly match a Lorentzian. The difference is due to the ideal brick-wall band-pass filter formed by the device. This is confirmed by the top-left graph which shows that the impulse response of the system is a 22 ps wide cardinal sinus, as expected for ideal band-pass filters.

Another interesting feature of the device is the ability to perform synthesis starting from a 6 GHz fundamental. This method allows to double the repetition frequency between pulses, but the lower number of harmonics produce a more approximated shape. Two examples of Lorentzian pulses with a 6 GHz fundamental are shown in figure 3.3.

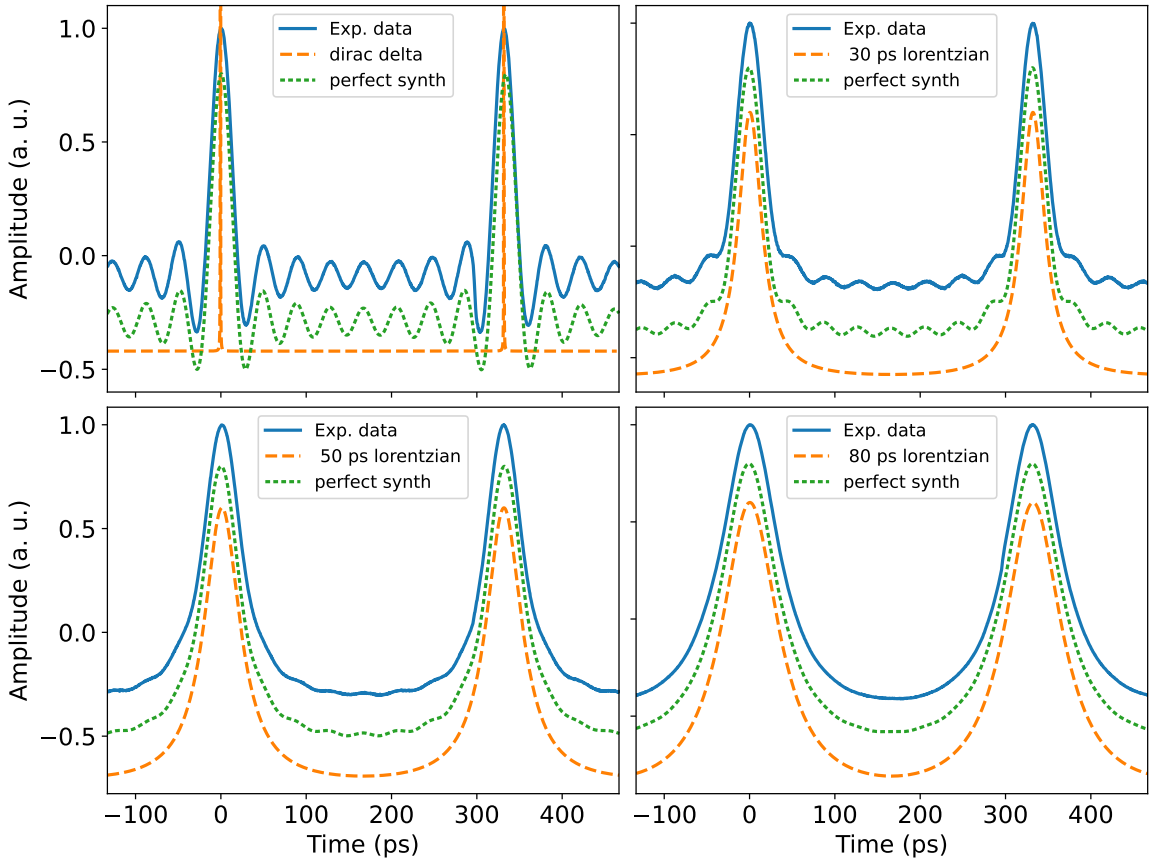

Figure 3.2: Pulse generator's outputs. From top left to bottom right: Lorentzian pulses with increasing width (FWHM). The measured output (blue), the theoretical best approximation that the device can perform (green) and the demanded Lorentzian pulse (orange). The curves have been shifted vertically for readability.

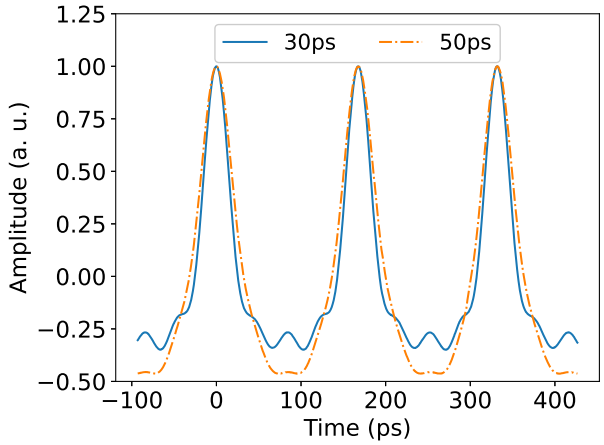

Figure 3.3: Synthesis with a 6 GHz fundamental. A repetition period of 166 ps can be observed.

3.3.1 Time stability

An important characteristic of the pulse generator is its ability to output a stable waveform during a long period of time. This is crucial in an experimental setup, as it is sometimes necessary to perform measurements over several hours or days.

In order to study the stability of the system, a 30 ps Lorentzian pulse has initially been synthesised and then measured every 10 minutes for 50 hours. With a discrete Fourier transform, the evolution of the amplitude of each harmonic has been extracted for each measurement. The results are shown in figure 3.4 (a), where a maximum relative variation of less than 2% can be observed. As the results of the measurement show a periodicity of 24h, these variations suggest an effect of changes in the ambient temperature in the laboratory. Controlling the temperature of the electronic components would allow to improve the stability even more.

Simply studying the evolution of the phase of the harmonics is not relevant to the study of stability, as a simple shift in time will add an extra phase without changing the waveform. To work around this effect, for every frequency a time delay is computed from the phase. The delays are then compared relatively to the 3 GHz fundamental. The results are shown in figure 3.4 (b), where a relative time drift between harmonics of less than 0.2 ps is demonstrated.

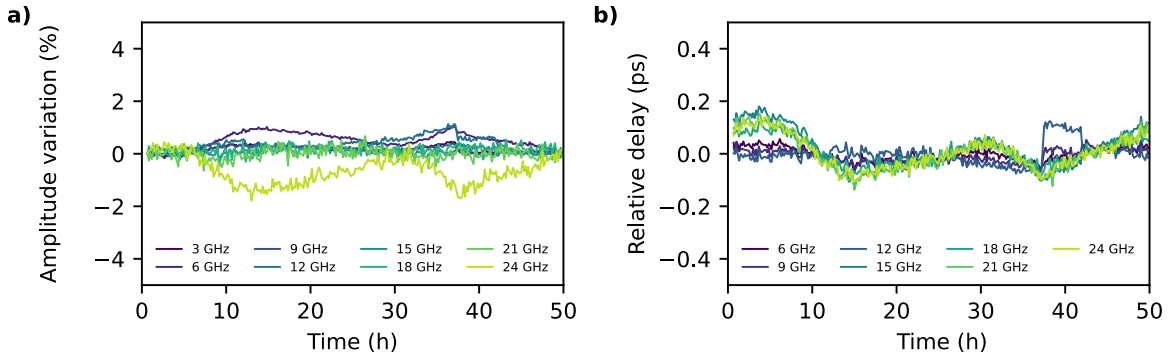

Figure 3.4: Long-time stability: a) relative time evolution of the amplitude of each harmonic. b) relative time delay between the higher harmonics and the 3 GHz fundamental. Adapted from [37]

In this chapter, the theory of Fourier synthesis has been presented alongside with our radio-frequency implementation. The ability to synthesise Lorentzian pulses from 20 ps to 80 ps has been demonstrated, and the stability of the output waveform has been studied. In the next chapter, a time resolved, in-situ measurement of the electronic wave packet generated by Lorentzian pulses will be presented.

Chapter 4

On-chip time-resolved pulse characterization

In the previous section, the ability to perform radio frequency Fourier synthesis of Lorentzian pulses with a temporal width down to 20 ps has been demonstrated. We will now present a in-situ, time-resolved characterisation of these pulses propagating in a 2DEG. Firstly, the working principle of the pump and probe technique will be explained, alongside with the experimental set-up. This is followed by the presentation of the experimental results.

4.1 Pump and probe

The characterization of an ultra-fast signal can prove to be difficult for multiple reasons. As the bandwidth of the signal is very large, it is not always possible to find an analog to digital converter (ADC) fast enough to correctly sample the waveform. Moreover, the electrical connection needed to bring the signal to the ADC might severely deform the shape of the pulse, as it will introduce attenuation, dispersion and multiple reflections. It is therefore necessary to exploit an ad-hoc technique able to perform the measurement locally.

Figure 4.1 schematically represents the pump and probe technique developed in [38] that has been employed for the characterization of our Lorentzian pulses. Let us consider a sharp pulse propagating along a conductor. Positioning an ON/OFF switch on the path of the propagating electron wave packet and briefly opening and closing the switch on a time scale shorter than the temporal width of the wave packet will allow to realise a time-resolved sampling of the wave packet. Changing the time delay τ between the sending pulse (pump) and the probing pulse (probe) and repeating the measurement several times allow to reconstruct the shape of the wave packet in a time-resolved manner, with a resolution that can be way lower than a picosecond.

In the pump and probe measurement, the incoming signal is sampled multiple

times at a specific delay. The samples are then measured with an integrator circuit, like a lock-in amplifier. With this technique, only a DC output is measured, and the dispersion or reflections along the conductors after the switch are not taken into account. This means that the pulse is reconstructed as it impinges on the switch.

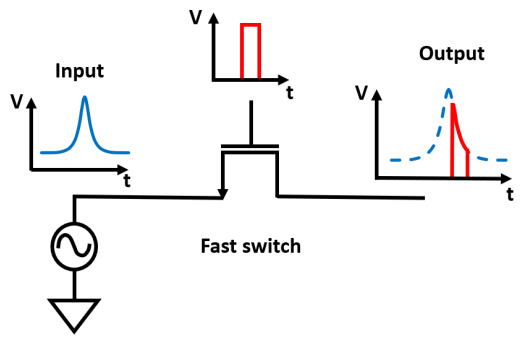

Figure 4.1: Schematic representation of the pump and probe measurement.

While incredibly powerful, the pump and probe measurements has two relevant downsides. Since it is very difficult to exactly compute or measure the transmission of a real switch, it is not possible to compute the exact amplitude of the incoming pulse and only the shape can be reconstructed. Secondly, the switch must be operated very fast in order to efficiently sample the the waveform and to reliably reconstruct its shape. When this is not the case, the measurement yield the convolution between the pulse and time dependent transmission of the switch. The real waveform can still be reconstructed by numerically deconvolute the signals.

4.2 2DEG implementation

We will now present the pump and probe set-up used to characterize an electron wave packet propagating through a 2DEG at cryogenic temperatures.

The sample used for this measurement is shown in figure 4.2 and consist of an electronic Mach-Zehnder interferometer (MZI) [39] realised with Shottky gates on a GaAs/AlGaAs heterostructure.

An electronic MZI works as follows. Electrons are injected from the top-left ohmic contact (yellow square) in the 2DEG. The electron travel to the first tunnel-coupled wire (TCW), where the wavepacket is split between the upper and lower channel. Next, the two wavepackets travel around the Ahronov-Bohm island (yellow). A perpendicular magnetic field induces, by Ahronov-Bohm effect, a phase difference between the upper and lower path. Finally, a TCW recombines the wavepackets.

Depending on the induced phase shift, the electron can show constructive or destructive interference with itself. In the first case, the electron will be detected as a current in the detection ohmic contacts (right yellow squares). In the second case, the electron will bounce back and it will be detected at the back-scattered ohmic contact (bottom-left yellow square)

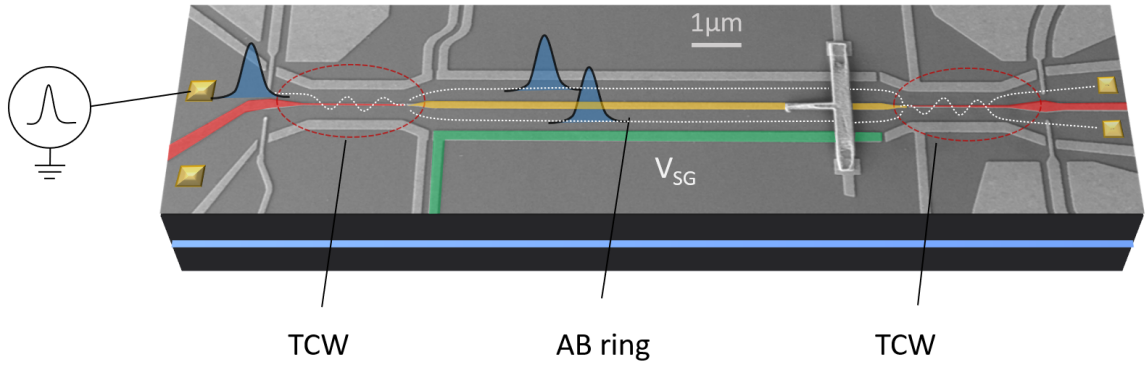

Figure 4.2: SEM image of the electronic Mach-Zehnder interferometer. The Shottky gates (light grey) are deposited on the surface of the GaAs (dark grey) and polarised to shape the 2DEG underneath (light blue). An electron wave packet (blue) is injected form the top left ohmic contact (yellow square, not in scale) and travels to the first tunnel-coupled wire (red), where it is split between to upper and lower path. A phase shift is induced by the Ahronov-Bohm effect in the central Ahronov-Bohm island (yellow). The wave packets are recombined with another tunnel-coupled wire and the electron is detected at the exit ohmic contacts.

To perform the pump and probe measurement, only the top half of the sample has been used. The Schottky gates have been polarized to form a one-dimensional channel. The fast switch is implemented by the quantum point contact [41] (QPC, yellow in figure 4.4) at the exit of the channel, and its operating sequence is shown in figure 4.3. The QPC is polarized with negative DC bias (roughly $-0.7\,\mathrm{V}$) in order to completely pinch off the 1D channel. When a voltage pulse is applied to the switch, the channel briefly opens allowing for partial transmission of an incoming signal. The negative DC bias is chosen in such a way that only the very tip of the pulse can open the channel. By doing this, the opening time of the switch is minimized.

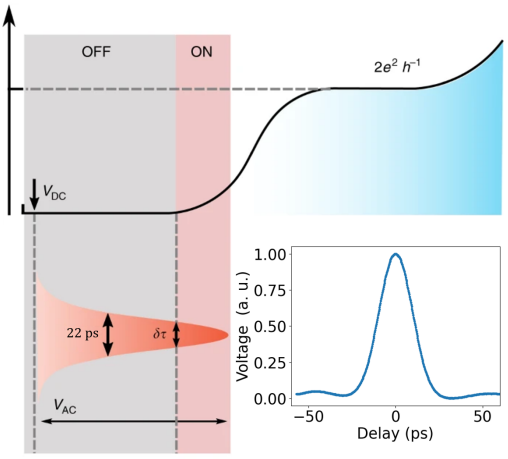

Figure 4.3: Operation of a QPC as a fast switch. The QPC is polarized with a strong negative bias in such a way that only the very tip of the applied voltage pulse can open the channel. Picture adapted from [40].

The measurement set-up is shown in figure 4.4. A voltage pulse is generated at room temperature with the device described in chapter 3. The pulse is then split into two output signals. Half is directly sent to the sample to actuate the QPC. The other half is firstly delayed by a room-temperature mechanical delay line, and is then sent to the cryostat, where it is attenuated before it finally reaches the 2DEG through the injection ohmic contact.

During the propagation in the 1D channel, the pulse is sampled by the QPC. The sample then propagates all the way to the detection ohmic contact, where it is integrated by a lock-in amplifier. The shape of the pulse in the 2DEG can then be reconstructed by simply plotting the voltage measured by the lock-in amplifier as a function of the delay. A 40 dB attenuator on the RF line is used to thermalise the electromagnetic wave that would otherwise heat up the sample.

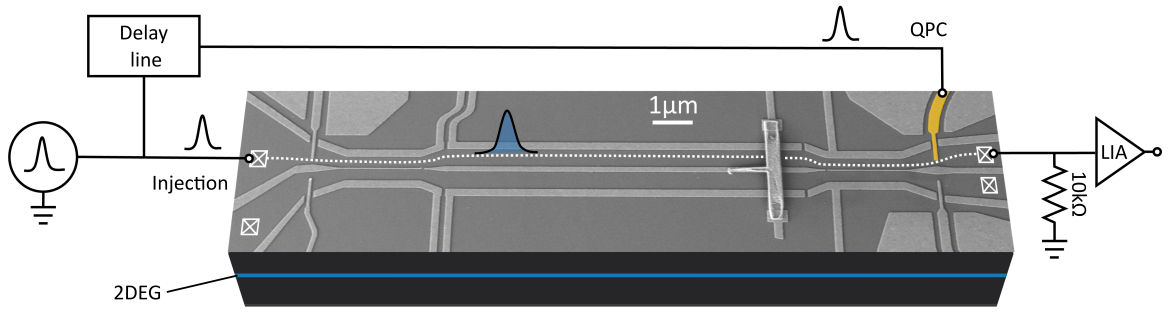

Figure 4.4: Measurement setup. The pulse generated by the signal generator is split in two. Half is used to operate the QPC (yellow). The other half is delayed, thermalized and injected in the 2DEG. By sweeping the delay, different samples of the propagating pulse can be obtained. The samples then propagate in the 1D channel (white dotted line) until the detection ohmic contact (white square) where they are integrated by a lock-in amplifier. Adapted from [37].

4.3 Results

In the following section, we will present the pump and probe measurements which have been performed on the sample shown in figure 4.2.

Firstly, we demonstrate the versatility of our pulse generator by measuring Lorentzian-like wavepackets with different widths and amplitudes. Figure 4.5 shows measured pulses with widths varying from 30 ps to 90 ps, while figure 4.6 demonstrates the control of the amplitude. Despite the generally good control and quality of the measured pulses, it has not been possible to completely compensate for the dispersion of the system and obtain a perfectly shaped Lorentzian. A similar limitation had not been observed in RF cables, where the dispersion of the system could be completely compensated. Further studies are needed to understand this limitation.

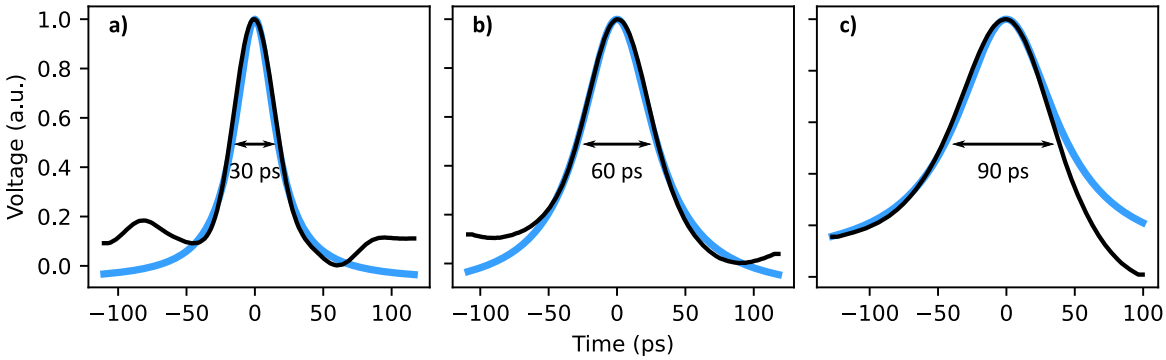

Figure 4.5: Electron wavepackets with varying width measured through the 2DEG. In black the experimental data, in blue the Lorentzian fit. Reproduced from [37].

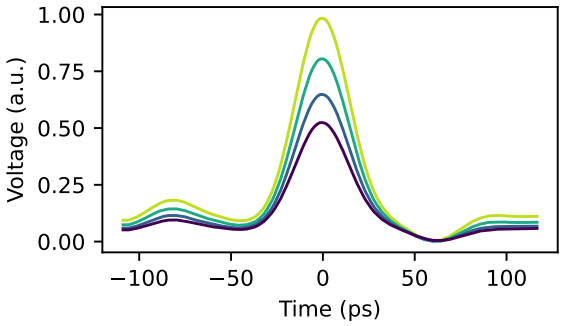

Figure 4.6: Electron wavepackets with varying amplitude measured through the 2DEG. Reproduced from [37].

Having shown the full control over the shape of the electronic wavepacket, we now demonstrate the ability to generate and measure record-short Lorentzian voltage pulses. A 25 ps wide pulse was deemed to be the shortest waveform that the device could generate while still maintaining a nice lorentzian line shape. In order to be able to observe a full period of the waveform, the fundamental frequency of the generator have been set to 6 GHz. This reduces the period of the signal from 333 ps to 166 ps, which is now below the maximum range of the mechanical delay line, limited to 230 ps. The results are shown in figure 4.7 (a) where a record width of 27 ps can be observed. The low width difference with the injected pulse of only 2 ps demonstrates that dispersion of our system is not severe and that the opening time of the QPC is negligible respect to the pulse duration. The inset of figure 4.7 (a) shows the frequency spectrum of the measured pulse. This spectrum is exponentially decaying with frequency as expected for lorentzian pulses.

With the measurement of a complete period of the electron wavepacket, we can now proceed to a theoretical prediction of its excitation spectrum. Equation 2.3 allows to compute the probability of an electron acquiring an energy ΔE from the voltage pulse.

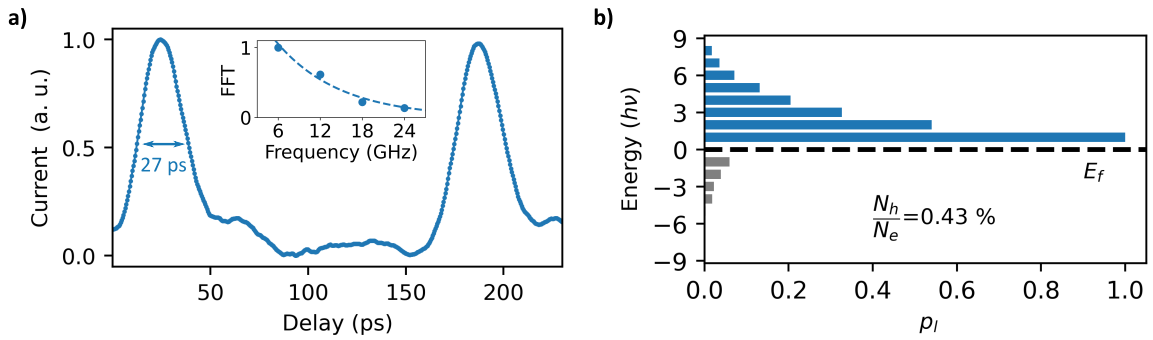

Figure 4.7: State of the art Lorentzian electron wavepacket measured in a 2DEG. (a) The measured wavepacket with a 27 ps width, only 2 ps longer than the generated pulse. The inset presents the frequency spectrum of the wavepacket, which exhibit the expected exponential decay. (b) Excitation probability computed for the measured pulse. The relative hole excitation have been evaluated to be 0.43%. Adapted from [37].

In our case, since the voltage drive is periodic, the extra phase factor in the electron wavefunction can be expressed more conveniently as a Fourier series [42]:

$$e^{-i\phi(t)} = \sum_{l=-\infty}^{+\infty} p_l e^{-i2\pi l\nu t}, \tag{4.1}$$

where ν is the repetition frequency of the signal and $|p_l|^2$ is the probability of the electron to absorb a photon of energy $lh\nu$. The p_l coefficient computed after numerically attenuating and biasing the electron wavepacket to the single electron regime are shown in figure 4.7 (b). The positive energies show the expected exponential decay typical of Leviton excitations, while the negatives energies, associated with hole excitations, shows small and quickly decaying amplitudes. The p_l coefficients can be further used to evaluate the excess hole excitation of the electron wavepacket. The number of holes (N_h) and electrons (N_e) generated in the Fermi sea by the voltage pulse can be computed as [42]:

$$N_e = \sum_{l=1}^{+\infty} l|p_l|^2, \tag{4.2}$$

$$N_h = \sum_{l=-\infty}^{-1} (-l)|p_l|^2. \tag{4.3}$$

The excess hole excitation of the wavepacket can than be evaluated as $\frac{N_h}{N_e} = 0.43\%$. While this is a remarkable results, it is important to keep in mind that this number has been computed for a temperature of 0 K. Quantum tomography experiments performed on similarly generated (although larger) wavepackets at T=60 mK [43], have demonstrated an excess hole excitation of 3 %. The larger hole excitation has been

completely linked to thermal fluctuations, and we therefore expect our wavepacket to behave similarly at comparable temperatures. In any case, we expect to be able to further reduce the zero temperature excess hole excitation by increasing the number of harmonics used by the signal generator and by better compensating for dispersion.

In this section we have presented the set-up used for the in-situ, time-resolved characterisation of ultra-short electron wave packets. While some work is still needed in order to precisely tune the amplitude of the waveform at the chip level, the ability to generate an electron wavepacket with very low spurious excitation has been demonstrated. Despite this remarkable result, voltage pulses of the order of tens of picoseconds are still too large to allow the up-scaling of the flying electron qubit architecture.

In the next chapter, we will address this point and present an alternative technique to generate voltage pulse as short as a picosecond.

Chapter 5

Optoelectronic conversion of femtoseconds pulses

In the previous sections, we have demonstrated the ability to generate and characterise leviton-like excitations with a temporal width of tens of picoseconds. While this is a remarkable result, even shorter pulses are needed to allow for the up-scaling of the flying-electron qubit architecture. As a control gate cannot be smaller than the electron wave packet, the spatial extension of the pulse must be reduced in order to implement as many gate operations as possible before coherence is lost.

In this section, we will present an alternative method, based on the optoelectronic conversion of optical femtosecond pulses, that allows for the generation of voltage pulses as short as a picosecond. Firstly, the generation of femtoseconds optical pulses will be presented. Then, we will explain how to perform the optoelectronic conversion of these short pulses by means of a photo-switch. Finally, we will present the experimental set-up used to generate these picosecond pulses and their characterisation.

5.1 Femtosecond laser

In order to generate ultra-short femtosecond optical pulses, we will exploit once again the Fourier synthesis. It is possible to show that by summing harmonics with the same amplitude and phase a Dirichlet kernel is obtained.

$$1 + 2\sum_{k=1}^{n} cos(kf_0t) = \frac{sin((n+1/2)f_0t)}{sin(f_0t/2)} \tag{5.1}$$

A few examples of Dirichlet kernel are shown in figure 5.1. These functions feature a very sharp peak, with a width $W = 1/nf_0$, repeated each $T = 1/f_0$.

In a laser, this synthesis can be implemented by choosing an active medium with a wide bandwidth. The cavity will be designed to sustain a large number of harmonics

of a fundamental mode. By forcing the harmonics to be in phase, the signal described in equation 5.1 is obtained. With a sufficiently large number of modes, an optical pulse

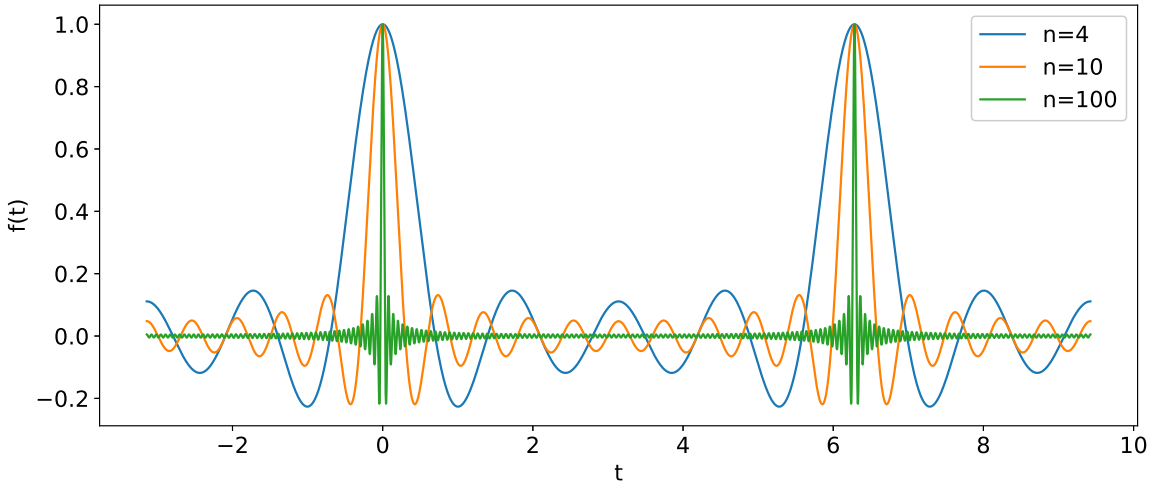

Figure 5.1: Example of Dirichlet kernels with different n.

with a width of a hundred femtoseconds can be generated [44]. Femtosecond lasers are widespread and commercially available.

5.2 Optoelectronic conversion

To convert a femtosecond optical pulse into an electric pulse, a photoswitch can be used [45]. An optical microscope image of the device is shown in Figure 5.2. It consists

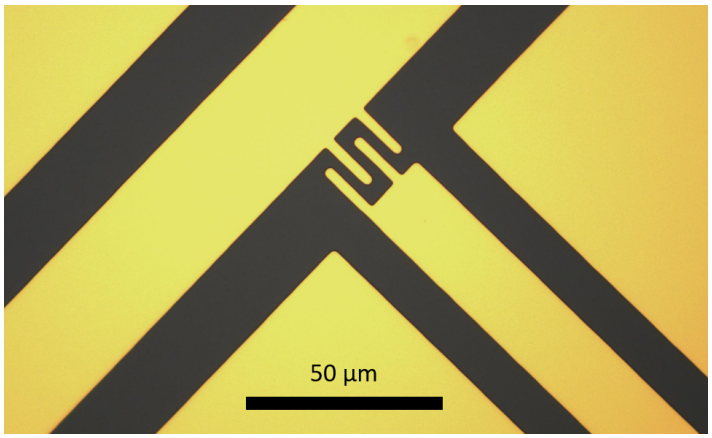

Figure 5.2: Optical microscopy image of a photoswitch. Two metal electrodes (yellow) are separated and electrically isolated by a layer of LT-GaAs (black). When an optical pulse impinges on the switch with a voltage bias, a current pulse is generated with a temporal width that is determined by the recombination time of the free carriers.

of two metallic electrodes deposited on a substrate of semiconducting material. In the OFF state the semiconductor is electrically insulating and does not allow for current to flow between the electrodes. When the switch is illuminated, carriers are generated in the semiconductor. If a bias voltage is applied between the two electrodes, a current will flow until the light is turned off and all the carriers have recombined. By pulsing the light source it is possible to generate current pulses through the switch.

The rising edge of the current pulse will be dependent on the width of the optical pulse while falling edge depends on the recombination time of the carriers. It is then crucial to use materials with a short recombination time. For this purpose, a special low-temperature-grown GaAs (LT-GaAs) has been developed [46]. This material presents a high density of defects that speed up carrier recombination to reach a carrier lifetime of 1 ps. With this technology we expect to generate electrical pulses with a temporal width of of the order of a picosecond.

5.3 Experimental set-up

We will now proceed with a description of the experimental set-up used to generate and characterise picosecond pulses. Once again, the pump and probe technique will be used.

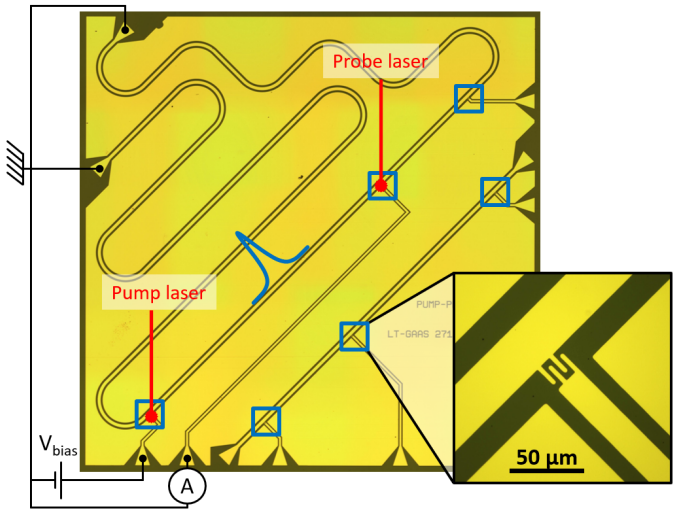

Figure 5.3: Electronic chip of the opto-electronic pump and probe setup. A coplanar waveguide is provided with three photo-switches (blue squares). One switch is biased and generates the electrical pulse when illuminated. The pulse then propagates on the waveguide to a second sampling switch, controlled by a delayed optical pulse. After being sampled, the waveform is integrated by a lock-in amplifier. By sweeping the delay between the pulses, the waveform can be reconstructed in a time-resolved manner.

The electronic chip used for the experiment is shown in figure 5.3. It consist of two coplanar waveguides, on which three photo-switches have been placed. One switch is biased and illuminated by a pump optical pulse to generate the electrical pulse. The pulse then propagates in the waveguide until another photo-switch is reached. A second laser pulse, which we will call the probe, opens the second switch at a controlled time delay, effectively sampling the propagating waveform. The output of the switch is integrated by a Lock-in amplifier. By changing the delay between the pump and probe pulses, the entire waveform of the generated pulse can be reconstructed in a time-resolved manner.

The optical setup used for the generation of the two optical pulses is shown in figure 5.4. A 70 fs pulse is generated with a repetition frequency of 250 MHz by the MenloSystems^{TM} C-Fiber 780 Laser. The pulse is then split in two with a beam splitter. Each beam is then sent through a mechanical delay line and an attenuator. Finally the beams are coupled to the optical fibers that will guide the pulses to the sample in the cryostat.

Due to the wide bandwidth of the signal, a large amount of dispersion is experienced by the pulses while travelling through the 8 m of optical fiber. To solve this problem, an optical compressor is placed before the beam splitter. This device consist of a series of two prism and two diffraction gratings that can completely compensate the second and third-order dispersion of the fibers [47].

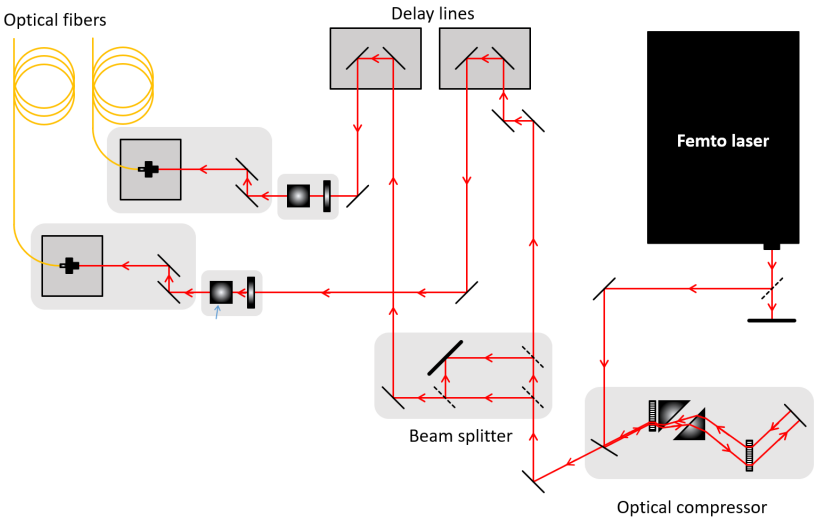

Figure 5.4: Schematic of the optical setup on the optical table. A pulse, generated by a femtosecond laser, is sent through an optical compressor to compensate for dispersion. The pulse is then split in two by a beam splitter. The two beams are sent to a mechanical delay line before being coupled to the optical fibers that will guide them inside the cryostat.

From the optical table, the fibers guide the pulses inside the cryostat all the way down to the cold finger, shown in figure 5.5. A lens focuses the two beams on the sample, with a relative distance of 1.25 mm between the spots. Since this distance cannot be controlled, the photo-switch must be placed on the chip exactly 1.25 mm apart.

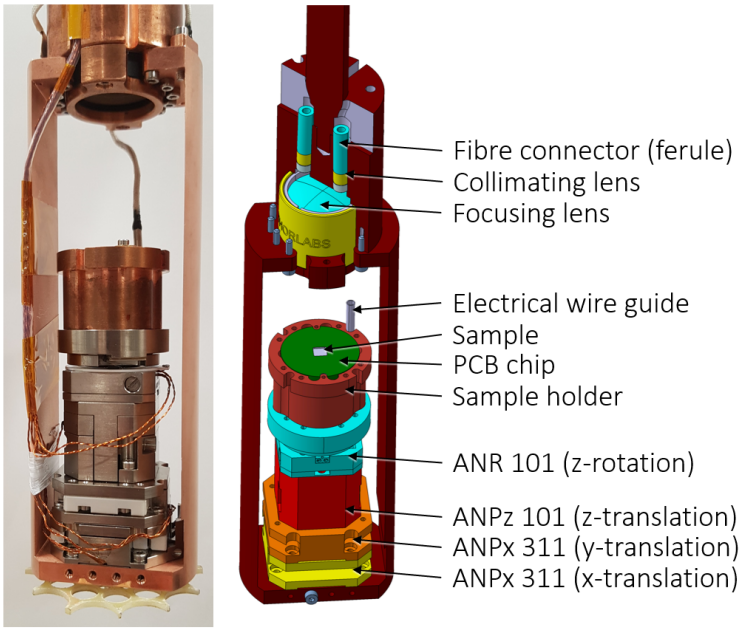

Figure 5.5: Picture and schematics of the cold finger. One can identify the optical fiber (light blue cilinders), the collimating lens (yellow cilinder), the sample PCB (green) and the piezoelectric stages (yellow, orange, red and light-blue boxes at the bottom)

To align the beams and the switches, four piezoelectric stages are inserted in the cold-finger to control the orientation of the sample on the X, Y, Z and R_z axis.

When cooling down the sample, thermal contraction causes small displacements in the position of the optical fibers and the lens. The focal plane of the beam is shifted up by 13 mm. The sample must then be moved to this position, where the relative distance between the spots is increased from 1.25 mm to 3.3 mm. In order to be able to perform measurement both at room temperature and 4K, an extra photo-switch has to be placed on the coplanar waveguide. In the future, the mechanical structure must be stabilised in order to use the same photo-switches at room temperature and at 4K.

5.4 Results

Pump and probe measurements have been performed on the sample both at room temperature and at 4K. The results are shown in figure 5.6. Both curves presents a 3 ps wide peak. In contrary to the pump and probe experiment performed in chapter 4, the opening time of the probe switch cannot be neglected, as its time response will be the same as the pump switch. The measured waveform is therefore the convolution of the pulse with itself. By taking this into account, a width of roughly 1.5 ps can be estimated for the voltage pulse travelling in the waveguide.

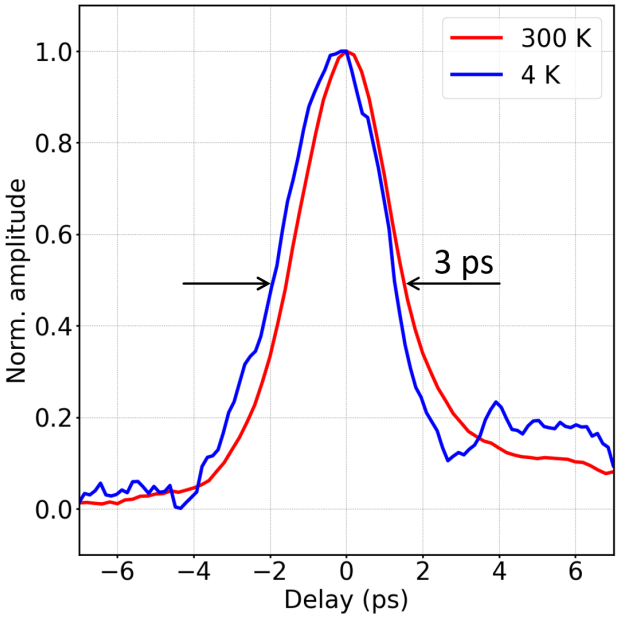

Figure 5.6: Pump and probe measurement of an optoelectronically-generated pulse. The measurement has been performed at 300K (red curve) and at 4K (blue curve). Both pulses show the same width of 3 ps.

While these optoelectronic pulses have a much shorter duration than the one generated with RF Fourier synthesis, which would make them perform better for quantum information applications, their waveform is not tunable. This means that, if the excitation spectrum of the pulses was found not to be pure enough, there would be no degree of freedom for further improvement. Moreover, the experimental implementation is extremely challenging, especially if a large number of source pulses is needed. Further work is still needed in order to properly apply these voltage pulses for single electron sources.

Chapter 6

Conclusions

In this work, different techniques for the generation of ultrashort electron wavepacket have been presented. Firstly, we have described and characterised a RF-based signal generator able to generate Lorentzian pulses as short as 20 ps. The device has been used to generate ultrashort electron wave packets inside a 2DEG. We have realised in-situ time-resolved characterisation of the propagating wave packets and demonstrated the ability to resolve a record-short 27 ps electronic excitation with an estimated spurious hole excitation of 0.43%. Finally we have presented an alternative technique for the generation of even shorter voltage pulses, based on the optoelectronic conversion of optical femtoseconds pulses. With this technique we have generated voltage pulses with a temporal extension down to one picosecond.

As mentioned in the introduction, the single electron source based on leviton generation is a promising candidate for application in quantum information technologies. Owing to the low energy of the electron and its proximity to the Fermi sea, the leviton is expected to have a long coherence time, which makes it suitable to be used as a source in an electronic Mach-Zehnder interferometer to realise a flying electron qubit.

Further work is still needed to precisely calibrate the amplitude and shape of the electronic wave packets at the chip level. Once this is achieved, the coherence properties of levitons will be investigated.

Bibliography

[1] Thomas N. Theis and H.-S. Philip Wong. "The End of Moore's Law: A New Beginning for Information Technology". In: *Computing in Science Engineering* 19.2 (2017), pp. 41–50. DOI: 10.1109/MCSE.2017.29.

[2] Michael A Nielsen and Isaac L Chuang. "Quantum computation and quantum information". In: *Phys. Today* 54.2 (2001), p. 60.

[3] Jeremy L O'brien. "Optical quantum computing". In: *Science* 318.5856 (2007), pp. 1567–1570.

[4] Stephan Ritter et al. "An elementary quantum network of single atoms in optical cavities". In: *Nature* 484.7393 (2012), pp. 195–200.

[5] Jiannis Pachos and Herbert Walther. "Quantum computation with trapped ions in an optical cavity". In: *Physical review letters* 89.18 (2002), p. 187903.

[6] Bruce E Kane. "A silicon-based nuclear spin quantum computer". In: *nature* 393.6681 (1998), pp. 133–137.

[7] Morten Kjaergaard et al. "Superconducting qubits: Current state of play". In: *Annual Review of Condensed Matter Physics* 11 (2020), pp. 369–395.

[8] Charles D Hill et al. "Global control and fast solid-state donor electron spin quantum computing". In: *Physical Review B* 72.4 (2005), p. 045350.

[9] C. Bäuerle et al. "Coherent control of single electrons: a review of current progress". In: *Reports on Progress in Physics* 81 (2018), p. 056503.

[10] Harry Levine et al. "High-fidelity control and entanglement of Rydberg-atom qubits". In: *Physical review letters* 121.12 (2018), p. 123603.

[11] Paul M Solomon and Hadis Morkoc. "Modulation-doped GaAs/AlGaAs heterojunction field-effect transistors (MODFET's), ultrahigh-speed device for supercomputers". In: *IEEE Transactions on Electron Devices* 31.8 (1984), pp. 1015–1027.

[12] W Walukiewicz et al. "Electron mobility in modulation-doped heterostructures". In: *Physical Review B* 30.8 (1984), p. 4571.

[13] J. Wang. "Surface acoustic waves as testbed for electron flying qubits". PhD thesis. Université Grenoble Alpes, 2022.

[14] John H Davies, Ivan A Larkin, and EV Sukhorukov. “Modeling the patterned two-dimensional electron gas: Electrostatics”. In: *Journal of Applied Physics* 77.9 (1995), pp. 4504–4512.

[15] Oktay Göktaş et al. “Alloyed ohmic contacts to two-dimensional electron system in AlGaAs/GaAs heterostructures down to submicron length scale”. In: *Physica E: Low-dimensional Systems and Nanostructures* 40.5 (2008), pp. 1579–1581.

[16] E. Bocquillon et al. “Electron quantum optics in ballistic chiral conductors”. In: *Annalen der Physik* 526 (2014), pp. 1–30.

[17] M. Yamamoto et al. “Electrical control of a solid-state flying qubit”. In: *Nature Nanotechnology* 7 (2012), pp. 247–251.

[18] Y. Aharonov and D. Bohm. “Significance of electromagnetic potentials in the quantum theory”. In: *Physical Review* 115 (1959), p. 485.

[19] S. P. Giblin et al. “Towards a quantum representation of the ampere using single electron pumps”. In: *Nature communications* 3 (2012), pp. 1–6.

[20] Mark David Blumenthal et al. “Gigahertz quantized charge pumping”. In: *Nature Physics* 3.5 (2007), pp. 343–347.

[21] JD Fletcher et al. “Stabilization of single-electron pumps by high magnetic fields”. In: *Physical Review B* 86.15 (2012), p. 155311.

[22] G. Yamahata et al. “Gigahertz single-electron pumping in silicon with an accuracy better than 9.2 parts in 10^7”. In: *Applied Physics Letters* 109 (2016), p. 013101.

[23] JD Fletcher et al. “Clock-controlled emission of single-electron wave packets in a solid-state circuit”. In: *Physical Review Letters* 111.21 (2013), p. 216807.

[24] M Büttiker, H Thomas, and A Prêtre. “Mesoscopic capacitors”. In: *Physics Letters A* 180.4-5 (1993), pp. 364–369.

[25] G. Fève et al. “An on-demand coherent single-electron source”. In: *Science* 316 (2007), pp. 1169–1172.

[26] D Ferraro et al. “Real-time decoherence of Landau and Levitov quasiparticles in quantum Hall edge channels”. In: *Physical Review Letters* 113.16 (2014), p. 166403.

[27] JM Shilton et al. “High-frequency single-electron transport in a quasi-one-dimensional GaAs channel induced by surface acoustic waves”. In: *Journal of Physics: Condensed Matter* 8.38 (1996), p. L531.

[28] S. Hermelin et al. “Electrons surfing on a sound wave as a platform for quantum optics with flying electrons”. In: *Nature* 477 (2011), pp. 435–438.

[29] R.P.G. McNeil et al. “On-demand single-electron transfer between distant quantum dots”. In: *Nature* 477.7365 (2011), pp. 439–442.

[30] G. Seelig and M. Büttiker. "Charge-fluctuation-induced dephasing in a gated mesoscopic interferometer". In: *Physical Review B* 64.24 (2001), p. 245313.

[31] Hermann Edlbauer et al. "Semiconductor-based electron flying qubits: review on recent progress accelerated by numerical modelling". In: *EPJ Quantum Technology* 9.1 (2022), p. 21.

[32] Benoit Gaury and Xavier Waintal. "Dynamical control of interference using voltage pulses in the quantum regime". In: *Nature Communications* 5.1 (2014), p. 3844.

[33] Mykhaylo Moskalets and M Büttiker. "Floquet scattering theory of quantum pumps". In: *Physical Review B* 66.20 (2002), p. 205320.

[34] L. S. Levitov, H. Lee, and G. B. Lesovik. "Electron counting statistics and coherent states of electric current". In: *Journal of Mathematical Physics* 37 (1996), pp. 4845–4866.

[35] DA Ivanov, HW Lee, and LS Levitov. "Coherent states of alternating current". In: *Physical Review B* 56.11 (1997), p. 6839.

[36] J. Dubois et al. "Minimal-excitation states for electron quantum optics using levitons". In: *Nature* 502 (2013), pp. 659–663.

[37] M. Aluffi et al. "Ultrashort electron wavepackets via frequency-comb synthesis". In: *arXiv preprint arXiv:2212.12311* (2022).

[38] G. Roussely et al. "Unveiling the bosonic nature of an ultrashort few-electron pulse". In: *Nature Communications* 9.1 (2018), p. 2811.

[39] Y. Ji et al. "An electronic mach–zehnder interferometer". In: *Nature* 422 (2003), pp. 415–418.

[40] E. Arrighi. "Time-resolved measurements of collective effects in quantum conductors". PhD thesis. Université Grenoble Alpes [2020-....], 2020.

[41] Hiroshi Kamata et al. "Voltage-controlled group velocity of edge magnetoplasmon in the quantum Hall regime". In: *Physical Review B* 81.8 (2010), p. 085329.

[42] Julie Dubois et al. "Integer and fractional charge Lorentzian voltage pulses analyzed in the framework of photon-assisted shot noise". In: *Physical Review B* 88.8 (2013), p. 085301.

[43] R. Bisognin et al. "Quantum tomography of electrical currents". In: *Nature Communications* 10.1 (2019), p. 3379.

[44] EA DeSouza et al. "Saturable absorber modelocked polarization maintaining erbium-doped fiber laser". In: *OSA Annual Meeting*. Optica Publishing Group. 1992, PD19.

[45] A. Johnson and D. Auston. "Microwave switching by picosecond photoconductivity". In: *IEEE Journal of Quantum Electronics* 11 (1975), pp. 283–287.

[46] F. W. Smith et al. “Picosecond GaAs-based photoconductive optoelectronic detectors”. In: *Applied Physics Letters* 54 (1989), pp. 890–892.

[47] N. Forget, V. Crozatier, and P. Tournois. “Transmission Bragg-grating grisms for pulse compression”. In: *Applied Physics B* 109 (2012), pp. 121–125.